

# Management of MRI Spatial Accuracy for Radiation Therapy

Teo Stanescu, Ph.D.; David Jaffray, Ph.D.

Princess Margaret Cancer Centre, University Health Network; Department of Radiation Oncology, University of Toronto, Toronto, ON, Canada

## Introduction

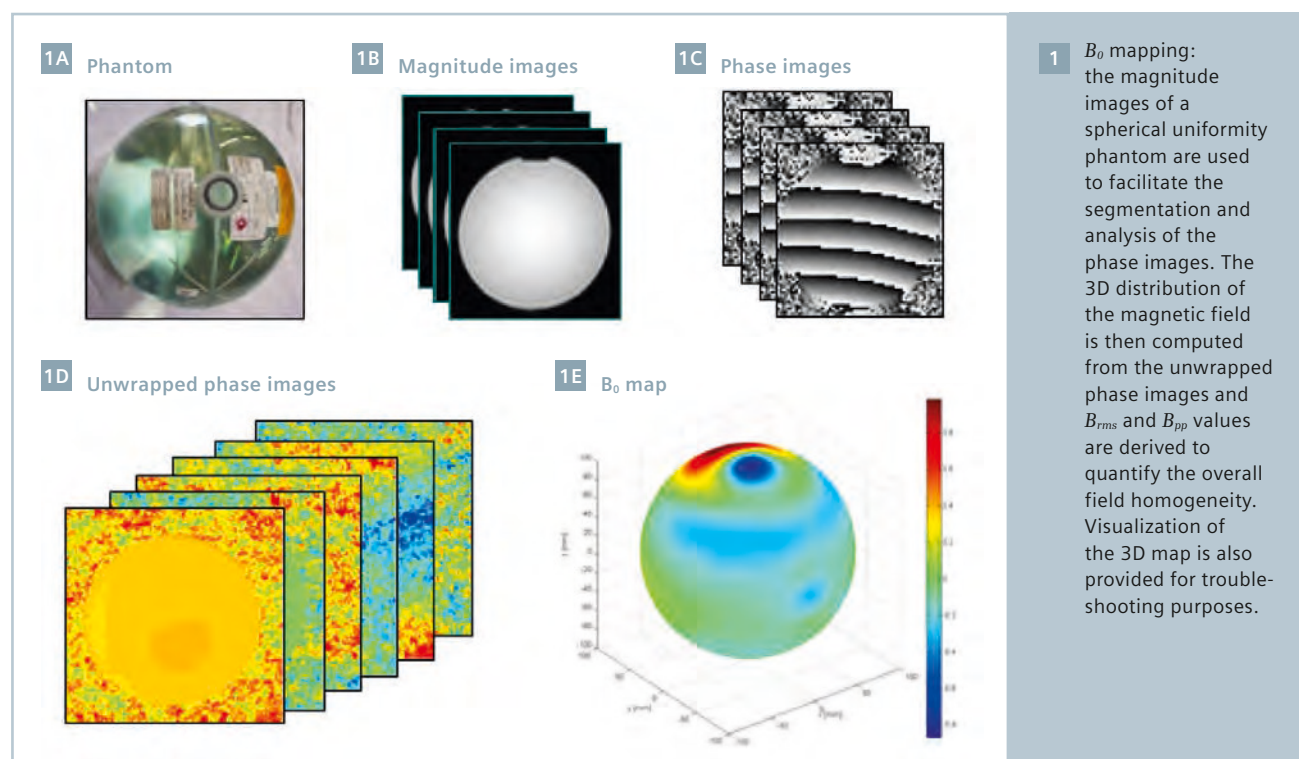
Radiation Therapy (RT) demands tight constraints regarding the geometric accuracy of image data used in its workflows for treatment simulation and in-room treatment delivery guidance. The spatial accuracy requirements are largely driven by the ability to deliver and deposit therapeutic radiation doses to targeted anatomical sites (1-2 mm). The benefits of MRI's superior soft-tissue contrast as compared to RT's gold standard based on x-ray imaging (i.e. CT, Cone Beam CT) are somewhat overshadowed by the intrinsic MR image distortions manifested as loss of

spatial accuracy and local intensity inhomogeneities.

The MR image distortions are given by a) scanner-related distortions caused by nonlinearities in the imaging gradients and inhomogeneities in the main magnetic field ( $B_0$ ), and b) patient-induced distortions mainly due to variations in the magnetic susceptibility properties of neighboring tissues (and chemical shift). The scanner-related distortion field ( $S$ ) is predictable, independent of the imaged subject and its spatial characteristics are static over time given optimal functionality of the MR system.  $S$  magnitude is negligible in the vicinity of the MR isocenter and

gradually increases with distance, reaching about 1-2 cm for large fields of views [1-3]. In comparison, the susceptibility-induced distortion field ( $X$ ) is highly dependent on the subject anatomy as they arise at the boundary between structures exhibiting local discontinuities in the susceptibility ( $\chi$ ) values, e.g. soft-tissue and air-filled cavities. The magnitude of  $\chi$  effects is in the range of a few millimeters and depends on several factors such as magnetic field and encoding gradient strength [4, 5].

A composite distortion field ( $C$ ) can be defined as the vector summation of  $S$  and  $X$ , to characterize the combined aspects of the two fields [6].  $S$  and  $X$



have negligible mutual coupling and can be treated independently following dedicated methodology. When  $C$  is associated with intrafraction motion, specific to mobile anatomical structures, it becomes more complex featuring 4D characteristics, e.g. for fast imaging 2D-cine, 4D MR. The quantification of  $C$  is then particularly challenging due to real anatomical changes in the targeted structure's volume, shape and relative location within the MR imaging volume. The accurate knowledge of a tumor's true contours during the motion cycle is paramount for advanced RT planning and delivery techniques which are based on radiation field gating or tracking [7, 8].

MR manufacturers made significant progress over the past years in implementing improved hardware and algorithms to reduce the magnitude of  $S$ . However, residual distortions are still an issue for RT applications [9]. Overall, the geometric distortions need to be well-understood for each MR-based technique and appropriate mitigation implemented to safely integrate MR data in radiotherapy workflows. Our work on the management of MR image distortions is motivated by the clinical implementation of MR-guided brachytherapy and external

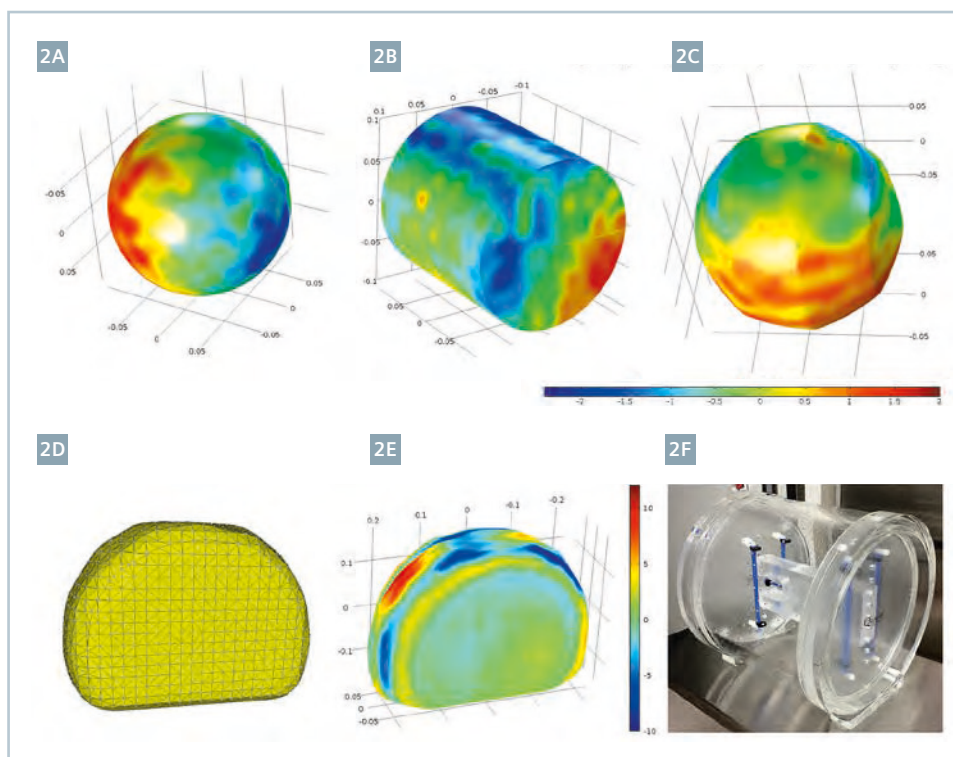
beam RT technologies and to enable MR-based adaptive procedures [10].

### Scanner-related distortions

Routine testing for monitoring the field homogeneity and its stability is recommended as a pre-requisite for good imaging. As part of our standard procedures for MR commissioning and periodic quality control (QC) of the system shim, we develop and implemented a fast  $B_0$  mapping technique based on a) phantom data acquisition with a GRE double-echo sequence and b) an image processing algorithm for data reformatting and phase unwrapping, and c) generation of analytics and reporting. The simplified flowchart is shown in Figure 1. First, magnitude and phase images are collected with a uniformity phantom. Then phase unwrapping is performed using the PUROR method [11] and metrics such as  $B_{rms}$  (root mean square) and  $B_{pp}$  (peak-to-peak) are computed and reported in a ready to print file. The image acquisition and post-processing was optimized to match the performance of the Phantom Shim Check procedure available in the Siemens service environment (1.5T MAGNETOM Espree, with software version syngo MR

B17A). The total time to scan and run the analysis on a mid-range PC workstation is under 100 seconds.

It is typical to quantify the gradient nonlinearities using a) a theoretical approach considering the spherical harmonics coefficients specific to each gradient set or b) via measurements with a linearity phantom. Although the theoretical approach is very appealing as it can be easily streamlined for image unwarping of live image data, it does not fully compensate for the image geometric errors [3, 9]. A phantom with a known structure, the most common being a 2D or 3D grid pattern, is desirable to measure the remainder of the distortions. In RT one of the requirements is to accurately define the anatomy for both small and large field of views, which means that the linearity phantoms should be able to provide enough spatial coverage. In particular, at large FOVs a phantom with a grid pattern needs to fill the entire volume to provide adequate sampling for  $S$ , which often translates into increased phantom weight. The manufacturing, routine preparation (positive or negative contrast) and manipulation of such a phantom may also be challenging.



**2** Harmonic analysis was applied to compute the 3D distortion vector field for an arbitrarily shaped volume from data measured on the surface. (2A) and (2B) show basic quadratic geometries; (2C) shows a Reuleaux 9-gon to test the method for a more complex structure; (2D) depicts the meshed and irregular surface of an MR imaging FOV as measured with a large phantom based on a grid design; (2E) the surface data corresponding to (2D) was used as BC in the harmonic analysis to stress-test its performance.

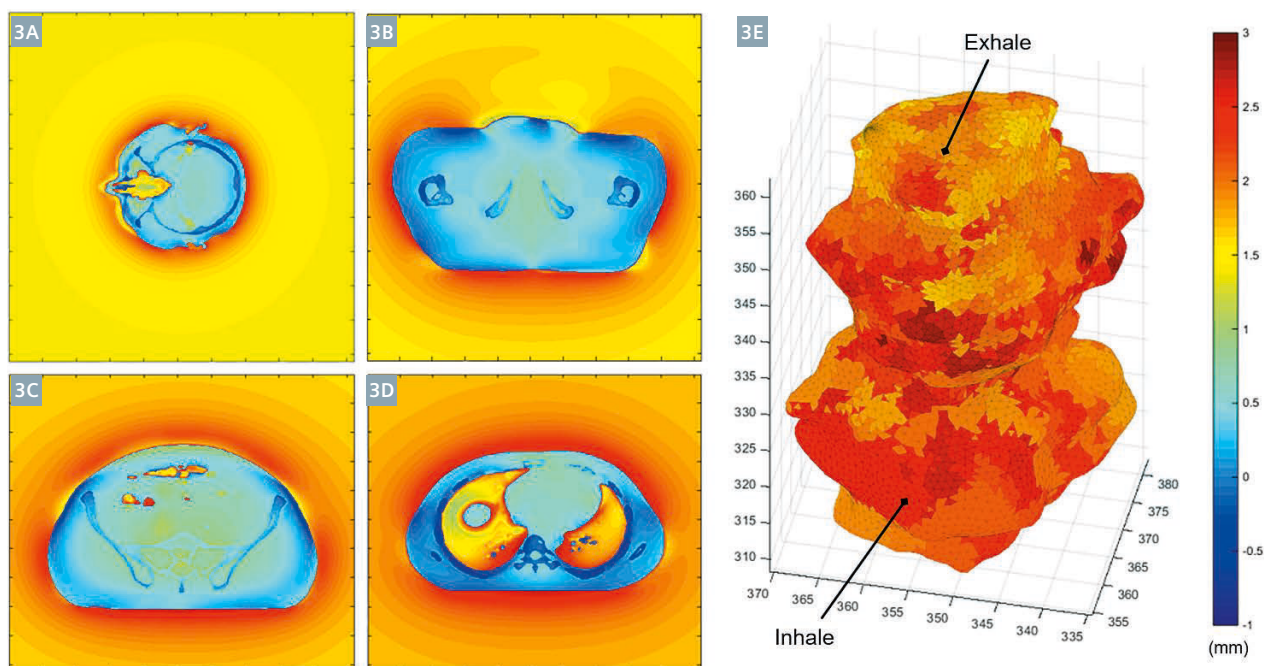
To address the above limitations our group focused on a design which minimized phantom material, weight and implicitly the manufacturing cost without compromising the accuracy in quantifying  $S$ . The design was driven by the ability to fully reconstruct  $S$  in a given volume solely from field data mapped on the geometry's surface [12]. This means that harmonic analysis can be applied to  $S$ , since  $S$  is natively related to the magnetic field. Specifically, the Laplace equation was solved with well-defined Dirichlet boundary conditions (BC) for functions representing the 3D geometric distortion vector field. The Dirichlet BCs were given by the measured vector field values corresponding to the domain's boundary. The method was validated for multiple quadratic and arbitrary geometries. In particular, Figure 2E depicts sample results for a general case of a highly irregular surface, which wraps the raw data measured on a grid phantom with a high density of control points. The case is

challenging due to the magnitude and local gradients specific to  $S$  at large FOVs. A cylindrical shell phantom and associated software application based on the harmonic analysis was developed in collaboration with Modus Medical Devices (London, ON, Canada) as shown in Figure 2F [13].

### Susceptibility-induced distortions

The field  $X$  is challenging to predict or quantify, especially when live image data is needed for the clinical decision making process. The map of tissue susceptibility-induced effects may change even for the same patient as a function of daily anatomy. Several methods were proposed in the literature to assess the  $\chi$  perturbations [5, 4, 15]. Rather than measure the susceptibility, which often requires additional image data leading to longer acquisitions times, we chose to investigate the  $\chi$  effects by means of numerical simulations

[4, 6]. A finite difference technique iteratively solves the Maxwell equations with associated BCs for the case of a time independent and uniform magnetic field (i.e.  $B_0$  of an MR scanner). The input data is given by 3D susceptibility maps synthetically generated by assigning bulk  $\chi$  values to anatomical structures delineated on CT image data sets. CT images were used to ensure the spatially true representation of the anatomy and to dissociate the  $\chi$  effects from other potential sources of geometric inconsistencies (e.g.  $B_0$  and  $B_1$  local inhomogeneities,  $S$ ). Magnetic field maps expressed in terms of ppm values were set as the output of the numerical computations. The spatial distortions (in mm) were then easily converted by specifying the  $B_0$  and readout gradient values ( $\Delta_{mm} = ppm \cdot B_0 / G_E$ ). Furthermore, the  $\Delta_{mm}$  values were interpolated and reported for the anatomical regions of interest. The simulation method was validated in phantom using a wide range of  $G_E$  values at 1.5T and 3T.



**3** Sample results of the magnetic field numerical computations performed to investigate the magnitude of  $\chi$  geometric effects. Multiple anatomical regions were simulated such as (3A) brain (whole skull), (3B) prostate, (3C) abdomen/upper GI, and (3D) lung. Inset (3E) shows the 4D composite distortion field results for a small and mobile lung tumor as estimated for the two extreme phases of the respiratory cycle, i.e. inhale and exhale.



Figure 3 shows several examples of  $X$  as modelled for specific anatomical sites. We found the data useful for at least two reasons: a) estimate the maximum boundary of the  $X$  effects for a given site and b) generate  $\Delta_{mm}=f(G_E)$  curves for  $B_0$  values of interest. The trends from b) were used to guide the optimization of clinical imaging protocols so that the geometric distortions were mitigated while the SNR penalty for increasing  $G_E$  was minimized. Therefore, our approach was to predict the  $X$  effects outcome for patient populations and compensate upfront whenever possible.

### 4D Composite distortion field

The raw MR images intrinsically embed the effects of both scanner-related and  $X$ -induced geometric distortions. The assessment of  $C$  for mobile tumors may be particularly non-trivial due to continuous variations in the local profile of the  $S$  and  $X$  fields as experienced by the tumors [6]. For example,  $S$  is static with respect to the MR scanner, but when seen from the mobile tumor's system of reference it becomes time-dependent as the target travels in regions with potentially different local  $S$  values. Therefore, a 4D characteristic may be associated with  $S$ . Similarly,  $X$  becomes 4D as the tumor deforms and changes location relative to surrounding anatomical landscape. To evaluate the upper boundary of the 4D composite field we combined the methodologies from above for  $S$  and  $X$  in the case of mobile lung tumors. The susceptibility simulations were performed for 10 separate 3D data sets representing individual phases of the breathing cycle as captured with 4D CT imaging.  $S$  was also derived for all tumor motion phases via vector field interpolation. Metrics such as max/mean/range and spatial perturbations in the tumor's center of mass were reported for the individual and combined fields. An example is shown in Figure 3E. The dominant contribution was from  $S$ , and it was suggested that a unique  $C$  correction (e.g. derived from one phase or a mean phase) may be applied to all tumor phases with negligible residual errors. For fast imaging,  $X$  was found largely negligible as a high BW is typically employed.

### Summary

The quantification of geometric distortions is needed especially for radiation therapy applications to ensure a high degree of image data accuracy. Knowing the true location of the targeted anatomy may enable the use of tighter treatment margins expected to improved tumor control through dose escalation and increased sparing of healthy tissues. The assessment of MR image distortions is recommended to be part of the MR scanner commissioning and routine quality control. The susceptibility effects may be minimized within acceptable thresholds in certain applications whereas the scanner-related distortions may be mapped via phantoms and unwrapped on patient data when relevant.

### References

- 1 D. Wang, W. Strgner, G. Cowin, D.M. Doddrell, R. Slaughter, "Geometric distortion in clinical MRI systems Part II: correction using a 3D phantom," *Magn. Reson. Imag.* 22(9):1223-32 (2004).
- 2 S.F. Tanner, D.J. Finnigan, V.S. Khoo, P. Mayle, D.P. Dearnaley, M.O. Leach, "Radiotherapy planning of the pelvis using distortion corrected MR images: the removal of system distortions," *Phys. Med. Biol.* 45:2117-2132 (2000).
- 3 S.J. Doran, L. Charles-Edwards, S.A. Reinsberg, M.O. Leach, "A complete distortion correction for MR images: I. Gradient warp correction," *Phys. Med. Biol.* 50(7):1343-61 (2005).
- 4 T. Stanescu, K. Wachowicz, D.A. Jaffray, "Characterization of tissue magnetic susceptibility-induced distortions for MRIGRT," *Med. Phys.* 39(12):7185-93 (2012).
- 5 R. Bhagwandien, M.A. Moerland, C.J.G. Bakker, R. Beersma, J.J.W. Lagendijk, "Numerical analysis of the magnetic field for arbitrary magnetic susceptibility distributions in 3D," *Mag. Res. Imag.* 12:101-107 (1994).
- 6 T. Stanescu, D. Jaffray, "Investigation of the 4D composite MR image distortion field associated with tumor motion for MR-guided radiotherapy," *Med. Phys.* (in press).
- 7 M.B. Tacke, S. Nill, A. Krauss, U. Oelfke, "Real-time tumor tracking: automatic compensation of target motion using the Siemens 160 MLC," *Med. Phys.* 37(2):753-61 (2010).
- 8 A. Sawant, R.L. Smith, R.B. Venkat, L. Santanam, B. Cho, P. Poulsen, "Toward submillimeter accuracy in the management of intrafraction motion: the integration of real-time internal position monitoring and multileaf collimator target tracking," *Int. J. Radiat. Oncol. Biol. Phys.* 74(2): 575-82 (2009).
- 9 A. Walker, G. Linley, P. Metcalf, L. Holloway, "MRI distortion: considerations for MRI based radiotherapy treatment planning," *Austral. Phys. Engin. Sci. Med.* 37(1):103-113 (2014).
- 10 D. Jaffray, M. Carlone, M. Milosevic, S. Breen, T. Stanescu, "A facility for magnetic resonance-guided radiation therapy," *Semin. Radiat. Oncol.* 24(3):193-5 (2014).
- 11 J. Liu, M. Drangova, "Intervention-based multidimensional phase unwrapping using recursive orthogonal referring," *Magn. Reson. Med.* 68(4):1303-16 (2012).
- 12 T. Tadic, D. Jaffray, T. Stanescu, "Harmonic analysis for the characterization and correction of geometric distortion in MRI," *Med. Phys.* 41(11):112303 (2014).
- 13 <http://modusqa.com/imaging/phantoms/mrid3d>
- 14 H. Chang and J. Fitzpatrick, "A technique for accurate magnetic resonance imaging in the presence of field inhomogeneities," *IEEE Trans. Med. Imaging* 11, 319-329 (1992).
- 15 M. Jenkinson, J. L. Wilson, and P. Jezzard, "Perturbation method for magnetic field calculations of nonconductive objects," *Magn. Reson. Med.* 52(3), 471-477 (2004).



Dr. David Jaffray



Dr. Teo Stanescu

### Contact

Teo Stanescu, PhD, MCCPM  
Assistant Professor  
Princess Margaret Cancer Centre  
610 University Avenue  
Toronto, ON, M5G 2M9  
Canada  
Phone (416) 946-4501 Ext. 5071  
[teodor.stanescu@rmp.uhn.ca](mailto:teodor.stanescu@rmp.uhn.ca)